Available online at www.sciencedirect.com
SCIENCE DIRECT®
International Journal of Multiphase Flow 32 (2006) 755–774
International Journal of Multiphase Flow
www.elsevier.com/locate/ijmulflow

Characterization of diabatic two-phase flows in microchannels: Flow parameter results for R-134a in a 0.5 mm channel

Rémi Revellin [a], Vincent Dupont [b], Thierry Ursenbacher [a], John R. Thome [a,*], Iztok Zun [c]

[a] *EPFL STI ISE LTCM, ME G1 464, Station 9, CH-1015 Lausanne, Switzerland*
[b] *Euro Heat Pipes S.A., B-1400 Nivelles, Belgium*
[c] *Faculty of Mechanical Engineering LFDT, University of Ljubljana, Askerceva 6, 1000 Ljubljana, Slovenia*

Received 1 August 2004; received in revised form 23 February 2006

Abstract

An optical measurement method for two-phase flow pattern characterization in microtubes has been utilized to determine the frequency of bubbles generated in a microevaporator, the coalescence rates of these bubbles and their length distribution as well as their mean velocity. The tests were run in a 0.5 mm glass channel using saturated R-134a at 30 °C (7.7 bar). The optical technique uses two laser diodes and photodiodes to measure these parameters and to also identify the flow regimes and their transitions. Four flow patterns (bubbly flow, slug flow, semi-annular flow and annular flow) with their transitions were detected and observed also by high speed video. It was also possible to characterize bubble coalescence rates, which were observed here to be an important phenomena controlling the flow pattern transition in microchannels. Two types of coalescence occurred depending on the presence of small bubbles or not. The two-phase flow pattern transitions observed did not compare well to a leading macroscale flow map for refrigerants nor to a microscale map for air–water flows. Time averaged cross-sectional void fractions were also calculated indirectly from the mean two-phase vapor velocities and compared reasonably well to homogeneous values.

Keywords: Microchannels; Flow patterns; Two-phase flows; Optical measurement technique

1. Introduction

In the interest of providing higher cooling capability for microtechnologies, the fundamentals of two-phase heat transfer in microchannels are being studied ever more extensively. Many two-phase flow and heat transfer prediction methods exist for vaporization inside macrochannels but these are not suitable to use for

* Corresponding author. Tel.: +41 21 693 5982; fax: +41 21 693 5960.
E-mail address: john.thome@epfl.ch (J.R. Thome).

0301-9322/$ - see front matter © 2006 Elsevier Ltd. All rights reserved.
doi:10.1016/j.ijmultiphaseflow.2006.02.016

microchannels due to small-scale phenomena. Therefore, research is underway to investigate these small-scale phenomena and characterize the two-phase flow process. The most important parameters controlling two-phase flow in microchannels are bubble frequencies, lengths and velocities, coalescence of bubbles, flow pattern transitions and void fractions. These will be measured and/or detected by an optical measurement technique developed specifically for this purpose.

To better predict heat transfer coefficients in microcooling elements and heat spreaders for electronic cooling, for example, it is desirable to develop a flow pattern map for predicting the flow regimes of two-phase flow in microchannels. Due to the predominance of surface tension over gravity forces, the tube orientation has negligible influence on the flow pattern. For this reason, in horizontal microchannels stratified flow (as verified by Triplett et al., 1999; Damianides and Westwater, 1988; Serizawa et al., 2002) does not exist. Slug flow also occupies a much larger range of vapor qualities when compared with large diameter channels (Wambsganss et al., 1993).

Among the first studies to describe flow patterns in microchannels is that by Suo and Griffith (1964). They denoted three different flow patterns in their study using channels of 0.514–0.795 mm: bubbly/slug, slug and annular flow. Similarly, the study of Cornwell and Kew (1992) also found three different flow patterns in rectangular channels (1.2×0.9 mm and 3.5×1.1 mm): isolated bubbles, confined bubbles, and slug/annular flow. Since then, many others have observed these three basic flow patterns: Sheng and Palm (2001) for 1–4 mm tubes, Damianides and Westwater (1988) for a 1 mm tube, Mertz et al. (1996) and Kasza et al. (1997) for a single rectangular channel of 2.5 mm by 6 mm, and Lin et al. (1998) using a single round tube of 2.1 mm inside diameter.

Some other authors describe microchannel two-phase flow using additional flow pattern designations, such as Triplett et al. (1999) using both rectangular and circular channels or Steinke and Kandlikar (2003) who found no difference in the theory used for macroscale channels. Yang and Shieh (2001) concluded their study on flow patterns of air–water and two-phase R-134a in small circular tubes by saying that none of the existing flow pattern maps were able to predict air–water and refrigerant flow pattern transitions in small tubes. Hetsroni et al. (2003) performed experiments for air–water and steam–water flow in parallel triangular microchannels. They emphasized the discrepancy between flow patterns of air–water and steam–water flow. Serizawa et al. (Serizawa and Feng, 2001; Serizawa et al., 2002; Serizawa, 2004) observed several distinctive flow patterns using air–water and steam–water flow in very small circular tubes of 20, 25, 50 and 100 μm diameter: dispersed bubbly flow, gas slug flow, liquid ring flow, liquid lump flow, annular flow, frothy or whispy annular flow, rivulet flow and liquid droplet flow.

The difficulty of identifying flow regimes and their transitions comes from the difficulties in obtaining good high speed images, in the interpretation of the flow (subjectivity and pattern definition depending on the author), and also in choosing the channel size that determines either macro or microscale or the transition between them. In this paper, the Confinement number ($Co = (\sigma/[gD^2(\rho_L - \rho_G)])^{0.5}$, where σ is the surface tension, g is the acceleration of gravity, D is the tube diameter and ρ_L and ρ_G, respectively, the liquid and vapor densities) is used as a criterion to distinguish if one is in presence of either micro or macroscale two-phase flow. As proposed by Kew and Cornwell (1997), the confinement is significant if $Co > 0.5$. In that situation, gravitational forces are negligible compared to surface tension forces. For R-134a at a saturation temperature of 30 °C, the threshold separating micro and macroscale is $D = 1.622$ mm. Fig. 1 shows elongated bubbles in 2.0, 0.8 and 0.5 mm channels to demonstrate that gravity has essentially no buoyancy effect for the 0.5 mm channel tested here.

The void fraction ε is also an important parameter used in heat transfer and pressure drop models. Only a few investigations have been carried out on this. Kawahara et al. (2002, 2005) used image processing to deter-

Fig. 1. Elongated bubble for three different channel diameters: (a) 2.0 mm channel; (b) 0.8 mm channel; (c) 0.5 mm channel.

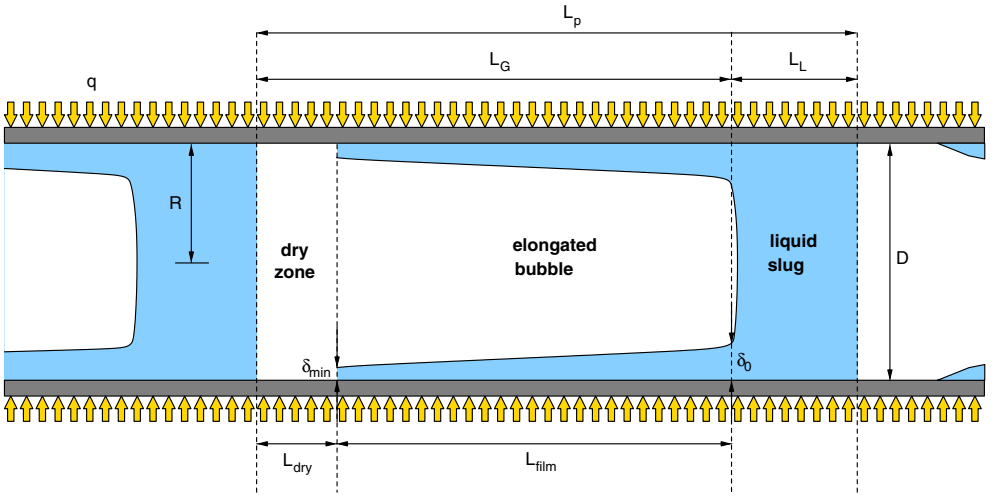

Fig. 2. Schematic of three-zone evaporation model.

mine the time-averaged cross-sectional void fraction. Their results for water-nitrogen in a 100 μm channel are far from the homogeneous model while instead their data for a 251 μm channel with ethanol–water/nitrogen are reasonably predicted by the Armand and Treschev (1946) correlation. Serizawa et al. (2002) made cross-sectional averaged void fraction measurements from high-speed video pictures and their data compared also reasonably well with the Armand and Treschev correlation.

Thome et al. (2004) and Dupont et al. (2004) proposed the first mechanistic heat transfer model to describe evaporation in microchannels with a *three-zone* flow boiling model that describes the transient variation in the local heat transfer coefficient during sequential and cyclic passage of (i) a liquid slug, (ii) an evaporating elongated bubble with a thin liquid film trapped between it and the channel wall and (iii) a vapor slug when film dryout has occurred as shown in the experiments of Xu et al. (2005), who used an infrared camera and a high speed video camera for studying boiling heat transfer of acetone flowing in ten parallel silicon microchannels with hydraulic diameters of 155.4 μm and observed the presence of intermittent dry zones. Cubaud and Ho (2004) also observed intermittent dry patches for liquid/gas flowing in 200 and 525 μm microchannels. Furthermore, heat transfer through the liquid films to bubbles also occurs in impinging jets, such as reported by Serizawa et al. (1990). Fig. 2 depicts a schematic of their three-zone heat transfer model. δ_{min} is the minimum liquid film thickness, δ_0 the initial liquid film thickness, L_G the length of the vapor bubble, L_L the length of the liquid slug, L_p the length of the pair (liquid slug/bubble), L_{dry} the length of the dryout zone, L_{film} the length of the liquid film, q the heat flux and R the radius of the tube. The new model illustrates the strong dependency of heat transfer on the bubble frequency, the lengths of the bubbles and liquid slugs, and the liquid film thickness, and is so far only applicable to the slug flow regime.

For these reasons, it is opportunistic to apply an optical measurement technique to quantitatively characterize flow pattern transitions, determine void fraction, and measure the frequency, velocity and length of vapor bubbles in microchannels, in particular at the exit of microevaporators in which the flows are formed. Such an optical measurement technique has been developed here and implemented in a new multi-purpose microchannel test facility and is presented in this article together with the new results.

2. Description of the test facility

A new experimental stand was built in order to control the fluid characteristics at the inlet of the test section, i.e. mass flow rate, inlet subcooling and saturation pressure. The test facility is shown in Fig. 3 and was designed with two optional methods for controlling the flow through the heat transfer and flow visualization test sections: (i) using a speed controlled micropump (*Pump mode*) and (ii) using the pressure difference between the upstream temperature-controlled refrigerant storage vessel (called also the hot reservoir) and

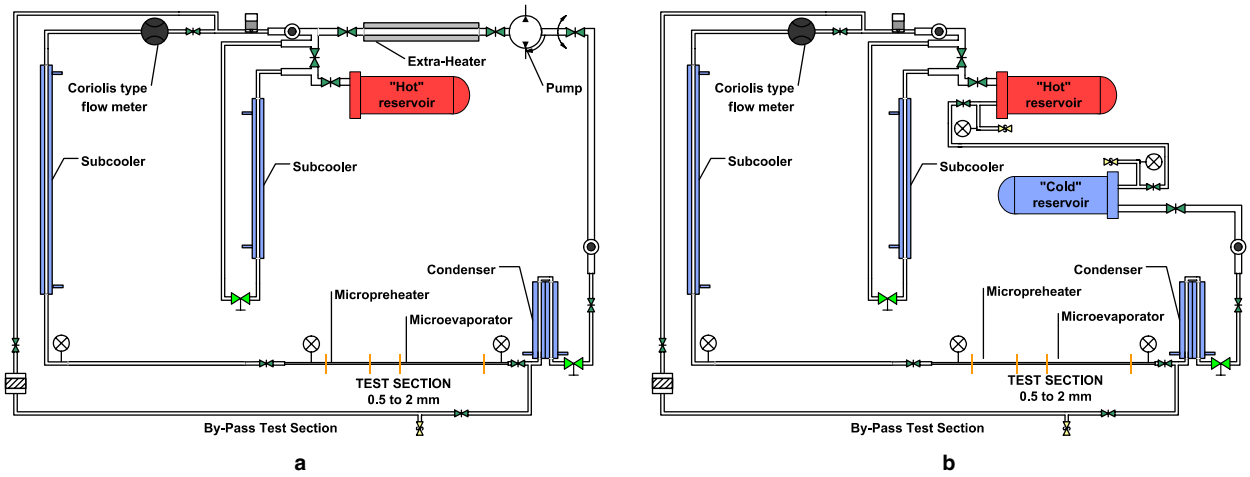

Fig. 3. Schematic of (a) pump loop and (b) reservoir loop.

its downstream companion (called also the cold reservoir) (*Reservoir mode*). A Labview interface has been created to control its operation and register measurements. A valve has been installed between the hot reservoir and the test section to avoid oscillations when boiling starts in the test section by increasing the pressure drop in the loop, so that back flow can be suppressed and a wider range of stable operations conditions achieved.

2.1. Test section

The test section consisted of an 80 mm long stainless steel tube used as a preheater, a 20 mm long glass tube for electrical insulation, a 110 mm long stainless steel tube heated section as the microevaporator and then a 100 mm long glass tube for flow pattern visualization and optical measurements, as shown in Fig. 4. The internal diameter of all these sections was 0.50 mm. Two copper clamps were attached to the preheater and to the evaporator. They were connected electrically to two Sorensen power supplies, respectively models DCS150-7E and DCS8-125E. They delivered direct current and heated the tubes by Joule effect. The vapor quality entering the flow visualization tube was calculated from an energy balance from the Joule heating at the outlet of the evaporator tube just before the glass visualization tube. Two pressure transducers were installed at the inlet and outlet of the test section as shown in Fig. 3 where the inside diameter is 4 mm. Two 0.25 mm thermocouples were placed in the fluid at the same locations. Four 0.25 mm thermocouples were also attached on the external surface of the microtubes in an adiabatic location (before the inlet and after the outlet of the preheater and the evaporator) to measure fluid temperature. Two more 0.25 mm thermocouples were installed on the two heated tubes to avoid dry out and overheating. All the test section was thermally insulated.

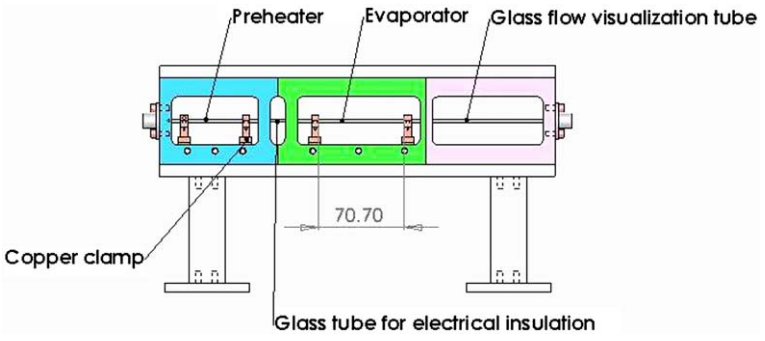

Fig. 4. Schematic diagram of the test section: front view.

Table 1
Experimental conditions

Parameter	Range	Units
D	0.50	mm
L (heated)	70.70	mm
G	350–2000	kg m^{-2} s^{-1}
q	3.7–129.7	kW m^{-2}
T_{sat}	30	°C
ΔT_{sub}	3	°C
x_{out}	0.4–85.2	%
$Re_L = G(1-x)D/\mu_L$	74–5340	–
$Re_G = GxD/\mu_G$	253–29020	–
$We_L = (G(1-x))^2 D/(\rho_L \sigma)$	0.04–220	–
$We_G = (Gx)^2 D/(\rho_G \sigma)$	0.03–864	–

It is of particular importance here to note that the present setup concerns actual two-phase flows exiting a microevaporator channel and not two-phase flows generated by a gas injector or liquid–vapor mixer. Hence, the bubbles observed here originated from nucleation in the evaporator and then flow downstream, just like in a microchannel cooling element attached to a computer chip, for instance. Thus, here the resulting flow pattern and bubble characteristics are determined by the process itself, not imposed or influenced by the design of the injector or mixer.

2.2. Experimental conditions and uncertainties

The experimental conditions are summarized in Table 1. L is the microevaporator length, G the mass flux, T_{sat} the saturation temperature at outlet to microevaporator, ΔT_{sub} the liquid subcooling at inlet to microevaporator, x_{out} the vapor quality at outlet to microevaporator, Re_L and Re_G, respectively, the liquid and vapor Reynolds numbers and We_G and We_L the vapor and liquid Weber numbers. Prior to the tests, energy balances were carried out on the test section for subcooled flow of R-134a. The difference in the energy balances between the liquid and the Joule heating diminished to within 2–3% for the maximum heat duties feasible for subcooled conditions, which are at the low end of heat duties for the evaporation tests. Hence, the energy balances (and the direct effect on local vapor qualities) are thought at worst to be ±2–3% but are probably ±1% for most of the two-phase conditions cited in Table 1. When running two-phase experiments, the R-134a arrives at the inlet of the preheater as a subcooled liquid. Then, it is heated to the desired temperature and enters into the evaporator to be partially evaporated. For the present tests, the reservoir mode was always used for driving the refrigerant as this gave the most stable flow.

A Coriolis mass flow meter was used to measure the mass flow rate ($\dot{m}$) of the subcooled R-134a to an accuracy of ±1% of the reading. The Joule heating was obtained by measuring the dc voltage by a *National Instruments* SCXI acquisition to an accuracy of ±0.02% and the dc current by a dc current transformer *Z202A* with an accuracy of ±3.5% for low currents and ±1% for high values. The absolute pressure transducers for monitoring the local pressures (P) were accurate to ±5 mbar. Thermocouples were accurate to ±0.1 °C. The vapor quality (x) entering the flow visualization tube was estimated to be accurate to ±1% for most test conditions. The pressure drops in the visualization tube reached up to 1.2 bar; this phenomena leads to an increase of the vapor quality along the tube from a flashing effect. The vapor velocity is by consequence increased due to this change of vapor quality. This variation of the vapor velocity is taken into account when processing the data (explained in the next part).

3. Optical measurement technique

An optical method to count bubbles and determine the two-phase flow characteristics has been used. The experimental setup consisted of two laser beams, with a power less than 1 mW, directed through the glass visualization tube and the fluid inside at two different locations, separated by a distance of $\Delta L_{Laser} = 70.63$ mm as presented in Fig. 5. Two lenses focused the laser beams to the middle of the microtube. Two photodiodes on

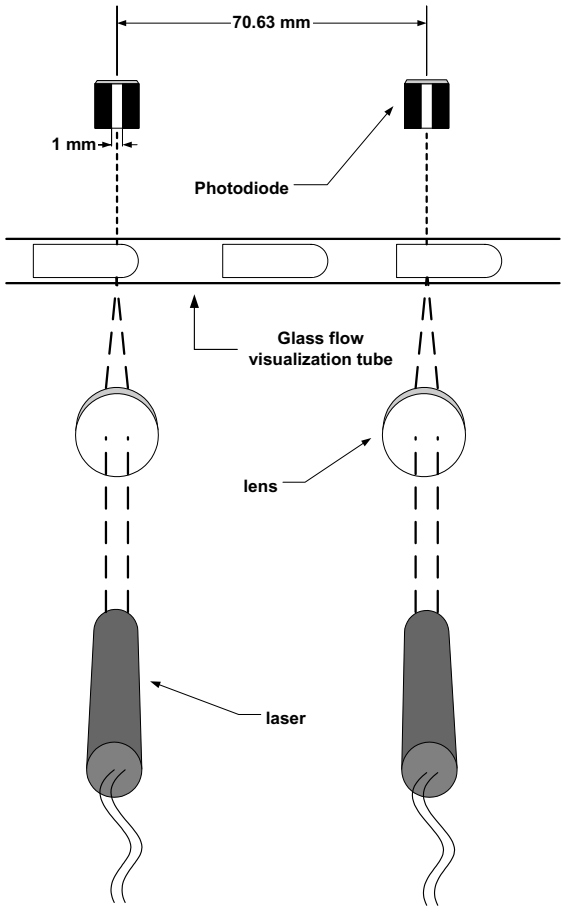

Fig. 5. Schematic diagram of the laser instrumentation.

the opposite side of the microtube, their faces painted over but leaving only a vertical 1 mm wide opening in the middle to isolate the signal, measured the intensity of the light. They were connected to a *National Instruments* SCXI acquisition system using a scan rate of 10,000 measurements/s to measure the resulting voltage signals from the two diodes. A micropositioning system was used to align the laser beams with the lenses and photodiodes. The laser beams interact locally with the structure of the flow and by signal processing, it was possible to determine the velocity, length and frequency of vapor bubbles. The signals from the diodes obtained by this technique for the different flow regimes are similar to those obtained by Lowe and Rezkallah (1999) using a void fraction probe for a microgravity air/water two-phase flow in a 9.525 mm tube.

The signal processing of our optical measurements consisted of several steps as follows:

Voltage thresholds: All flow patterns, as for example shown for slug flow in Fig. 6, yielded pulsed signals with peaks characterizing the vapor phase and troughs characterizing liquid phase. Only in the case of a slug flow, the count rate of peaks corresponds to the count rate of troughs for the same time count period, providing that the thresholds are set at a level that avoids noise either on the liquid or on the vapor signal. Fig. 6 shows an example of a histogram obtained by this method derived from its corresponding diode voltage signal. To count vapor bubbles, thresholds were determined in volts after first segregating the diode voltage signal into 5 mV steps, 20 mV after the first peak for threshold A and 40 mV before the second peak for threshold B. Threshold A is −440 mV for this example and threshold B is −345 mV. When the voltage signal is below threshold A, the presence of liquid is detected. Signals greater than threshold B mean that an annular flow or an elongated bubble is present. Between these two thresholds, either the nose or tail of a bubble or a frothy mix of liquid and vapor is present. These threshold values were kept constant for each

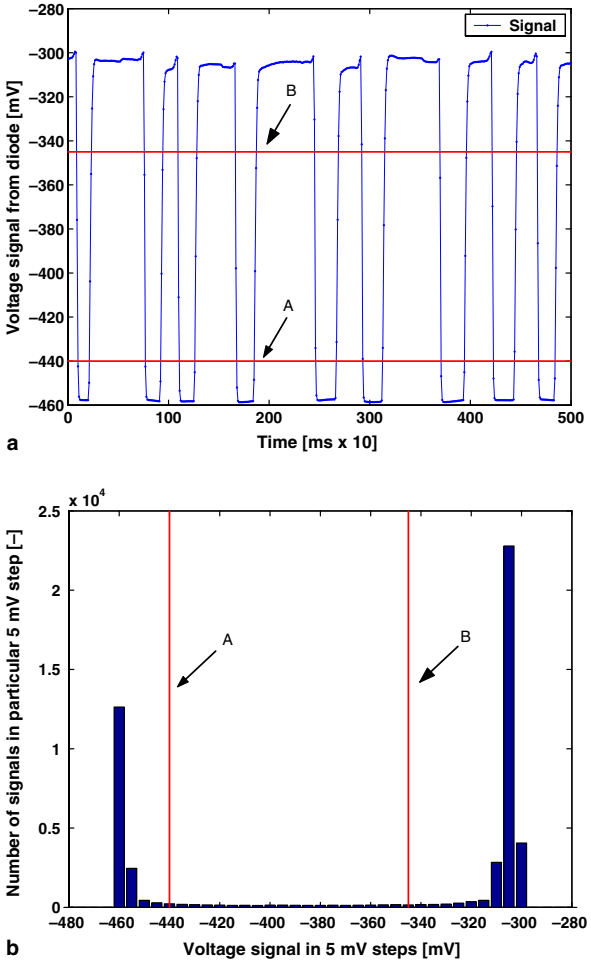

Fig. 6. Example of (a) a voltage signal and (b) a histogram of its distribution showing the chosen thresholds for characterizing a slug flow. (a) Signal from diode versus time and (b) histogram of 50,000 voltage signals segregated into 5 mV steps.

experimental condition but varied a little due to the periodic repositioning of the lasers, photodiodes and lenses and thus were reexamined for each set of results.

Vapor bubble frequency: The program counts the number of times the voltage is less than the threshold A and divides by the elapsed time period of 5 s for each test. This count rate is called average frequency f_A. The program counts also the number of times the voltage is above the threshold B and divides by the time period. This gives the sum of the elongated bubble frequency and the semi-annular frequency, the latter which is annular flow with churn transition zones in place of the liquid slugs when present. This count rate is called average frequency f_B.

Vapor bubble velocity: The method to determine the vapor bubble velocity is based on that developed by Matthes et al. (1970). For the fixed distance of 70.63 mm between the two lasers, only the signals for slug types of flow were able to be cross-correlated as shown in Fig. 7. From time delay between the two signals defined by the peak location, one may calculate the average velocity of elongated bubbles.

An image processing program has also been developed with Matlab to double check the velocity determined by the two lasers versus video images. The video camera is a high definition CCD camera. Fig. 8 shows an image with the vapor bubble lighted by a strobe. It is possible to determine the velocity of the nose of the bubble by knowing the time delay of the strobe light (Δt_{strobe}) and the distance covered by the bubble during this time period. To calculate this distance, the program determines the number of pixels

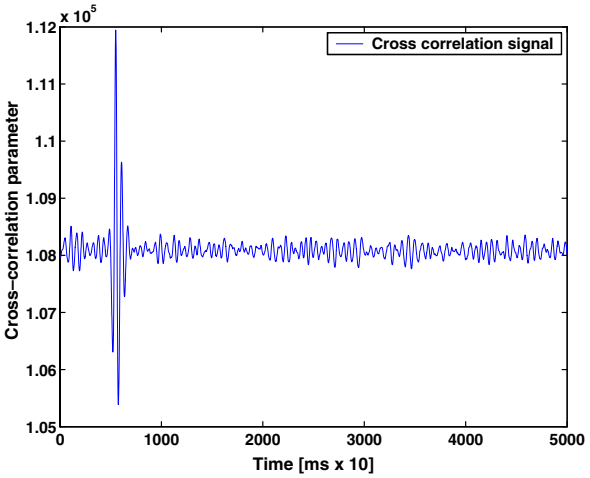

Fig. 7. Example of cross-correlation of voltage signals from the two diodes.

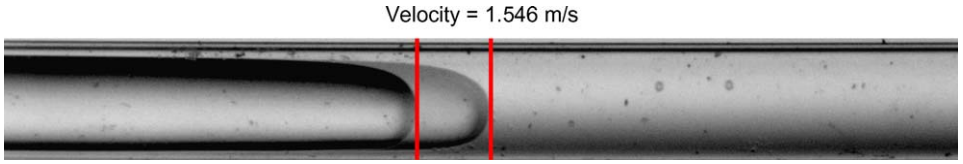

Fig. 8. Image used for laser calibrating for $D = 0.5$ mm, $L = 70.48$ mm, $G = 525$ kg m^{-2} s^{-1}, $T_{sat} = 35$ °C, $x_{out} = 9.63\%$, $\Delta T_{sub} = 5$ °C, $\Delta t_{strobe} = 2.8$ ms.

between the two bubble fronts (or backs) and at the same time the number of pixels for the outside diameter of the tube (whose diameter is 0.722 mm ± 3.5%). Then the distance covered by the vapor bubble is known and the velocity is obtained.

To implement the comparison, 100 images have been taken by the high definition camera. After treatment and using the properties of the Gauss law, the mean velocity is $U_{video} = 1.698$ ms^{-1} with an estimated error of ±19%. The signal processing gives a velocity of $U_{laser} = 1.517$ ms^{-1} with an estimated error of ±3%. Taking into account the respective uncertainties, these results are in good agreement. The laser signal velocity calculation was thus validated for slug flow and is the preferred measurement method because of its higher accuracy and its faster data processing rate.

The effect of the pressure drop in the sight glass on the vapor velocity (flashing effect) is taken into account by using simultaneously Eqs. (1) and (2) based on mass conservation applied on a small volume of vapor as shown in Fig. 9 where z is the longitudinal abscissa, $\dot{m}_G$ the vapor mass flow and $\dot{m}_{flash}$ is the vapor mass flow due to the flashing effect. Eq. (1) is used to incrementally calculate the local vapor velocity $U_G(z + dz)$ from laser 1 to laser 2, assuming the initial value of U_G(laser 1) at z. Then the mean (U_{mean}) is calculated using Eq. (2) and compared to the value at the midpoint between laser 1 and 2. The iterative procedure thus gives the values of U_G at laser 1 and 2 from the known vapor density (which varies with the pressure drop) and an assumed void fraction model that gives ε_G

$$U_G(z+dz) = \frac{\rho_G(z)\varepsilon_G(z)U_G(z)}{\rho_G(z+dz)\varepsilon_G(z+dz)}\left[\frac{x(z+dz)}{x(z)}\right] \quad (1)$$

$$U_{mean} = \frac{U_G(\text{laser 1}) + U_G(\text{laser 2})}{2} \quad (2)$$

The void fraction was assumed to be homogeneous in the above calculation.

Vapor bubble length: By knowing the vapor bubble velocity (i.e. U_{laser}) and time that a vapor bubble needs to cross the laser signal, its length can be calculated. When a bubble is smaller in length than the internal

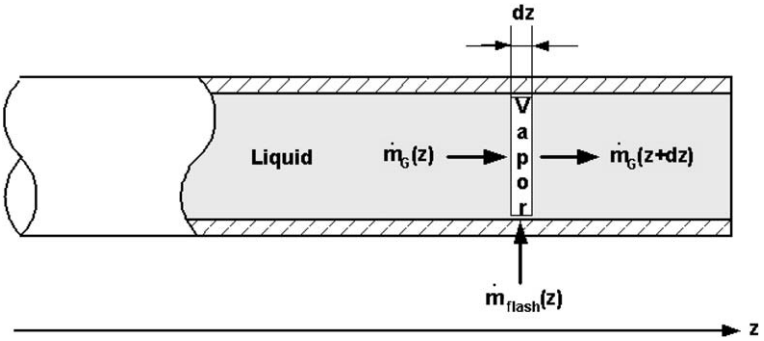

Fig. 9. Small element of vapor used for vapor velocity calculation.

diameter of the microchannel, it is classified as a *small* bubble; otherwise, it is defined here as an *elongated* bubble.

4. Experimental results

4.1. Vapor bubble velocities

Fig. 10 shows vapor bubble velocities from laser 2 plotted versus the thermodynamic vapor quality at that location. Here, mean vapor velocities calculated from the homogeneous void fraction equation have also been plotted from the following expression:

$$U_{\mathrm{Hom}} = G_{\mathrm{total}}\left[\frac{x}{\rho_{\mathrm{G}}} + \frac{1-x}{\rho_{\mathrm{L}}}\right] \tag{3}$$

where U_{Hom} is the homogeneous velocity and G_{total} the total mass flux.

In general, the comparison shows that the vapor velocity is close to that of homogeneous flow at low vapor qualities and deviates from this model at higher vapor qualities. The vapor velocity is close to homogeneous for small vapor bubbles or small vapor slugs that flow near the wall since they are slowed down due to the velocity profile in the boundary layer. This phenomena tends also to deform the shape of the vapor bubble

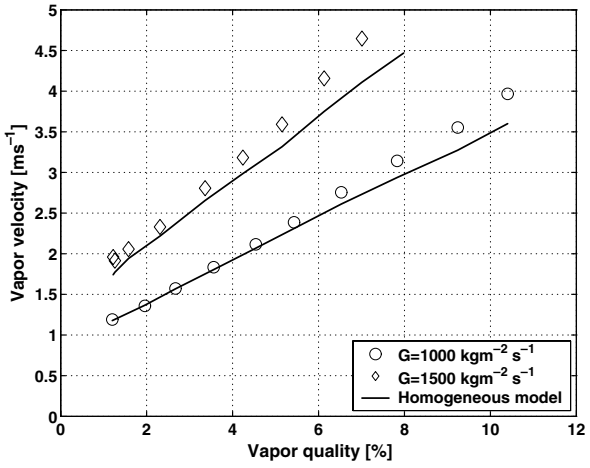

Fig. 10. Vapor velocity versus vapor quality from laser 2 for $D = 0.5$ mm, $L = 70.70$ mm, $T_{\mathrm{sat}} = 30$ °C, $\Delta T_{\mathrm{sub}} = 3$ °C at inlet to evaporator for slug and slug/semi-annular flows.

as can be observed in the video images shown in the next section. Furthermore, the channel is horizontal and hence there is no buoyancy effect to lift the bubble as in slug flows in vertical channels.

4.2. Flow patterns

Four principal flow patterns and two intermediate transition regimes have been observed in the present study. Only three principal flow patterns (bubbly flow, slug flow and annular flow) were able to be identified by FFT of pulsed signals, as shown in Fig. 11, but these signals were not sufficient to identify the transitions. While bubbly flow exhibited almost white noise in FFT, slug flow was characterized by periodic frequencies between 80 and 170 Hz in this particular case. Annular flow was characterized by a dominant frequency smaller than 30 Hz. Semi-annular flow however does not exhibit a characteristic trace to be distinctively recognized by FFT signal processing alone, but the difference between the bubbly flow and the semi-annular signals can be determined by also comparing their raw signals (shown later) and has been verified by flow visualization using a high speed camera. By examining the evolution of peak and trough count rates versus vapor quality, it was possible to determine the rate of coalescence of small bubbles into elongated bubbles and even elongated bubbles into semi-annular flow. The transitions were thus in fact detected by count rates of signal peaks and troughs on the A and B thresholds and by the percentage of small bubbles remaining as shown in Fig. 12 and not the ambiguous FFT signals. The microscale flow patterns observed are defined as follows:

Bubbly flow: In bubbly flow, the vapor phase is distributed as discrete bubbles in a continuous liquid phase and the bubbles are smaller in length than the diameter of the tube as shown in Fig. 13a. This regime is detected when the percentage of surviving small bubbles is 100% and their average frequency f_A is greater than 0 bubbles/s. This flow pattern covers a very small range of vapor quality and is more or less nonexistent at high mass flux. Fig. 14a shows a picture taken with a high definition video camera and Fig. 15a shows the voltage/time signal of the diode for this flow with the periodic passage of small bubbles. The average frequency f_A of bubbles here is 34 bubbles/s.

Bubbly/slug flow: In bubbly/slug flow, bubbly flow (described above) and slug flow (described below) are both present as shown in Fig. 13b. It is detected when the percentage of surviving small bubbles is in the range from 1% to 99% and average frequency f_A is greater than 0 bubbles/s. Fig. 14b shows a picture taken with a high definition video camera and Fig. 15b the corresponding signal. The average frequency f_A increases rapidly with the heat flux in the evaporator, reaches a peak and then decreases due to coalescence of small and elongated bubbles.

Slug flow: In slug flow, the vapor bubbles are approximately the same diameter as the tube as shown in Fig. 13c. The nose of the bubble has a characteristic hemispherical cap and the vapor in the bubbles is separated from the tube wall by a thin film of liquid. The liquid flow is contained mostly in the liquid slugs which separate successive vapor bubbles. The length of the vapor bubbles can vary considerably. This flow pattern is detected when the percentage of surviving small bubbles is 0%, f_B is the same as f_A and f_A is still greater than 0 bubbles/s. Fig. 14c shows a picture taken with a high definition video camera and Fig. 15c the corresponding signal. In this signal, the low voltage zones refer to passage of liquid slugs and the small amplitude spikes represent small bubbles entrained in the slugs (if any); on the other hand, the high voltage zones refer to passage of elongated bubbles and variations in the signal correspond to interfacial waves on the liquid film. The count rates decrease with increasing vapor quality due to coalescence of elongated bubbles but at a slower rate than in the case of small bubbles.

Slug/semi-annular flow: In slug/semi-annular flow, the slug (described above) and semi-annular (described below) flows are both present. The vapor velocity increases with heat flux and the rear of elongated bubbles are more and more deformed, see Figs. 13d and 14d as shear forces are more and more important. When coalescence occurs, transitions are no longer clean but instead create a churn-like zone where the liquid slug was. This regime is distinguishable when the signal is between threshold A and B as shown in Fig. 15d. This transition starts when f_A and f_B are not the same and stops when f_A equals 0 bubbles/s corresponding to the maximum of f_B.

Semi-annular flow: In semi-annular flow, liquid slugs are nonexistent as shown in Figs. 13e and 14e. A liquid film forms at the tube wall with a continuous central vapor core. It is separated by churning liquid zones

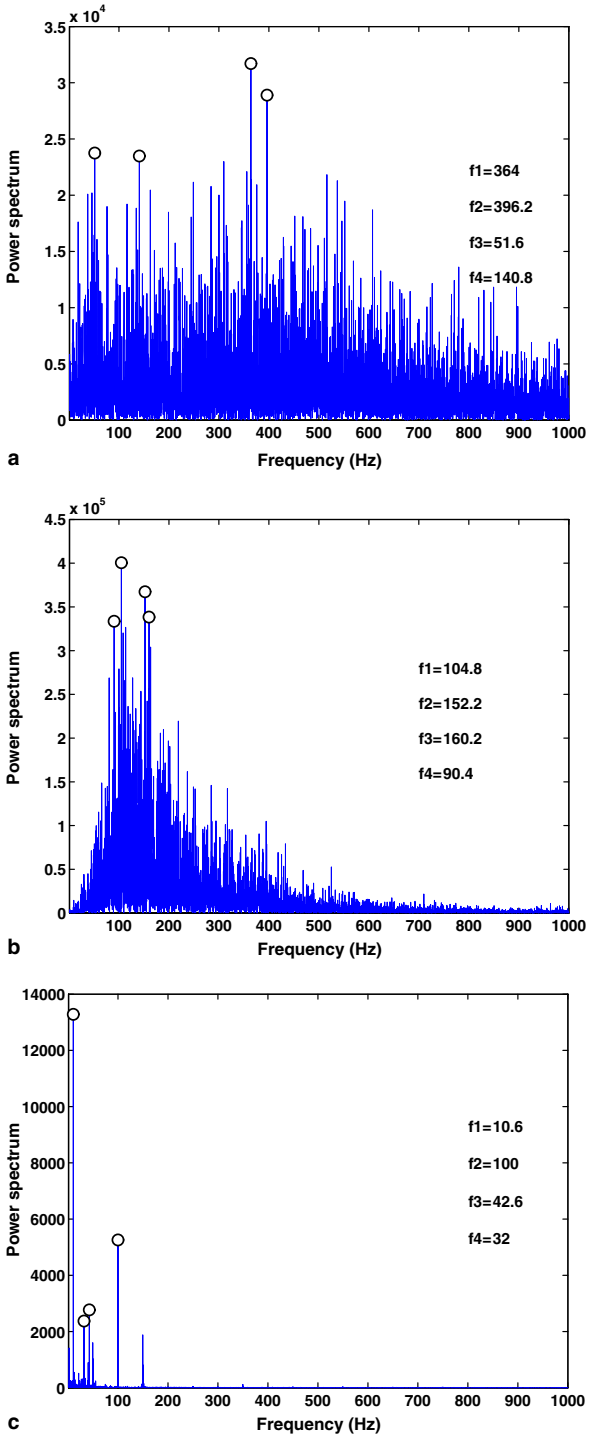

Fig. 11. FFT signals for $D = 0.5$ mm, $L = 70.70$ mm, $G = 500$ kg m^{-2} s^{-1}, $T_{sat} = 30$ °C and $\Delta T_{sub} = 3$ °C at inlet to evaporator: (a) FFT signal on bubbly flow for $x = 2\%$; (b) FFT signal on slug flow for $x = 11\%$; (c) FFT signal on annular flow for $x = 82\%$.

due to the previous deformation of the rear ends of elongated bubbles and the coalescence of bubbles. This flow pattern is represented by the signal of Fig. 15e. Limits of this transition are the end of

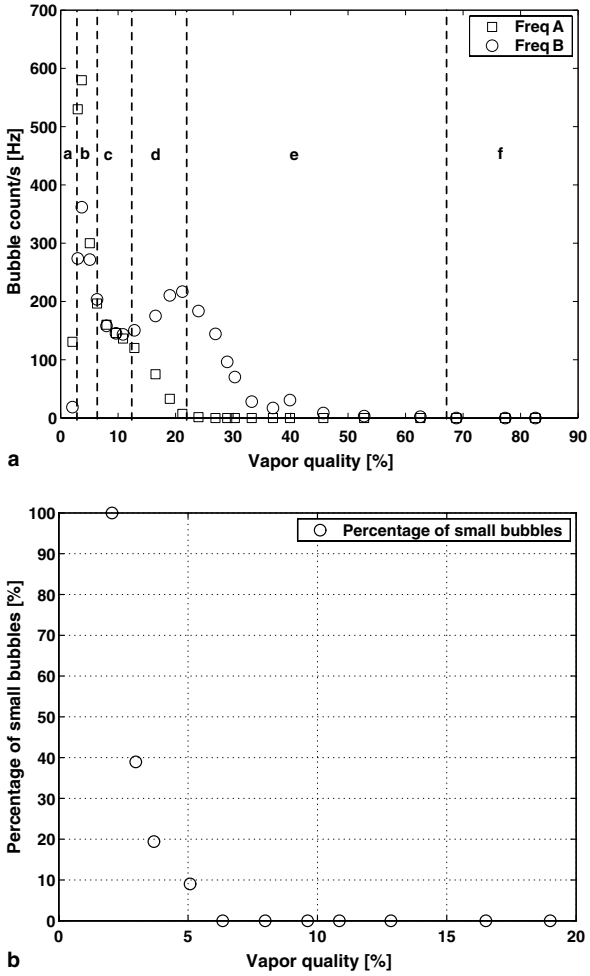

Fig. 12. Characterization of flow using laser signal. (a) Bubble frequencies and flow patterns and (b) percentage of small bubbles remaining versus vapor quality for $D = 0.5$ mm, $L = 70.70$ mm, $G = 500$ kg m^{-2} s^{-1}, $T_{sat} = 30$ °C and $\Delta T_{sub} = 3$ °C at inlet to evaporator. (a) a: Bubbly flow, b: bubbly/slug flow, c: slug flow, d: slug/semi-annular flow, e: semi-annular flow, f: annular flow.

slug/semi-annular flow and the beginning of annular flow, which is indicated by a value of f_B equal to 0 Hz. It is interesting to emphasize that the churning liquid disappears gradually from the beginning of this transition up to the end.

Annular flow: In annular flow, a liquid film flows on the tube wall with a continuous central vapor core as shown in Fig. 13f. It is the same definition as for semi-annular flow, except that the churning liquid zones do not exist anymore. Annular flow is characterized by f_A and f_B equal to 0 Hz. The corresponding identification signal is shown in Fig. 15f and illustrates two types of annular flow: wavy and smooth, where the wavy annular flow signals have a small scale fluctuation from the waves on the annular film. The higher the vapor quality, the longer the smooth annular part is. These two types of annular flow can be seen in Fig. 14f and g.

It is interesting to emphasize here that the relative symmetric configuration of the flow confirms the predominance of surface tension forces over gravitational forces. The confinement is thus significant for $D = 0.5$ mm and R-134a at a saturation temperature of 30 °C.

Two-phase flow patterns based on the present observations with the two laser signals are presented in Fig. 16 in two different formats: mass flux versus vapor quality and superficial liquid velocity versus superficial vapor velocity, which are calculated from the test results as follows:

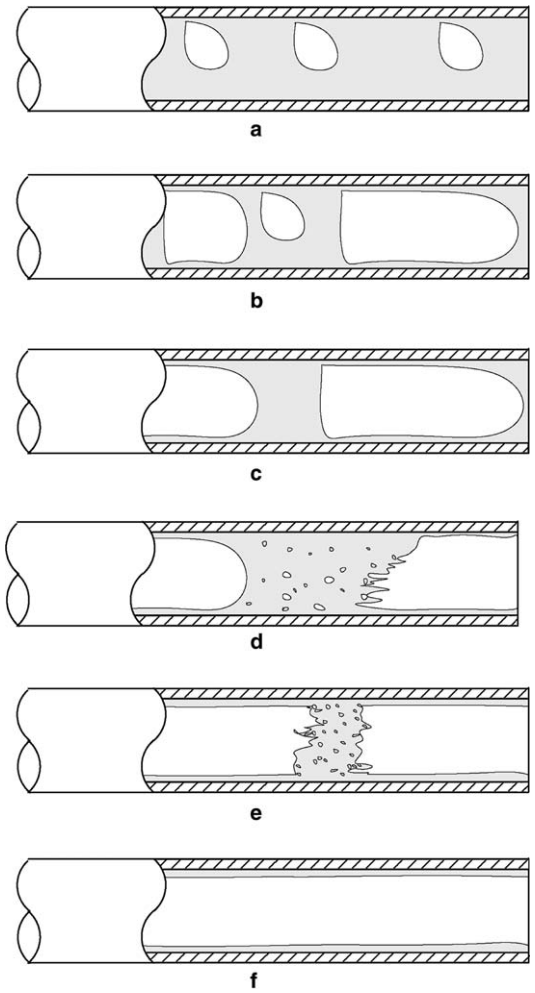

Fig. 13. Schematic of flow patterns and transitions: (a) bubbly flow; (b) bubbly/slug flow; (c) slug flow; (d) slug/semi-annular flow; (e) semi-annular flow; (f) annular flow.

$$J_L = \frac{(1-x)G}{\rho_L} \tag{4}$$

$$J_G = \frac{xG}{\rho_G} \tag{5}$$

where J_L is the liquid superficial velocity and J_G the vapor superficial velocity.

Notably, the higher the mass flux, the earlier annular flow is reached. Bubbly flow is more or less nonexistent for mass fluxes greater than 1000 kg m^{-2} s^{-1}. The most important observation to make about the flow patterns in the present study is that their transitions are controlled primarily by the rate of coalescence, which is not recognized as a contributing factor by any of the microscale (nor macroscale) flow pattern maps. A comparison with the macroscale map of Kattan et al. (1998) for refrigerants shows a significant difference in the transition line locations and also the flow patterns encountered (Fig. 17a), illustrating that the current observations cannot be classified as macroscale two-phase flows. Fig. 17b shows a comparison between the present experimental transition lines from laser 1 and those of Triplett et al. (1999) available for air/water flow in a 1.097 mm tube diameter; the results are not in good agreement when extrapolating their air–water map to R-134a.

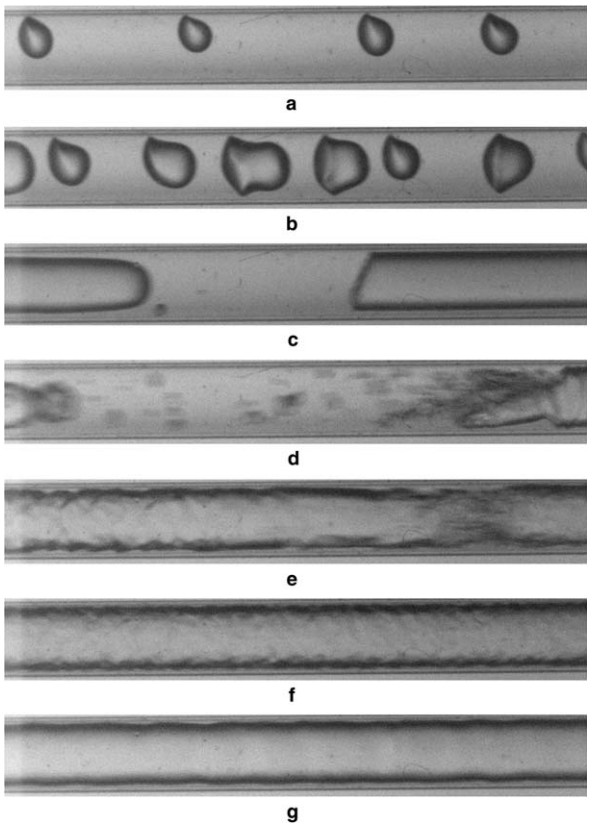

Fig. 14. Flow patterns and transitions for $D = 0.5$ mm, $L = 70.70$ mm, $G = 500$ kg m^{-2} s^{-1}, $T_{sat} = 30$ °C and $\Delta T_{sub} = 3$ °C at entrance to heater: (a) bubbly flow at $x = 2\%$ and $f_A = 131$ Hz; (b) bubbly/slug flow at $x = 4\%$ and $f_A = 520$ Hz; (c) slug flow at $x = 11\%$ and $f_A = 136$ Hz; (d) slug/semi-annular flow at $x = 19\%$ and $f_A = 33$ Hz; (e) semi-annular flow at $x = 40\%$ and $f_A = 0$ Hz; (f) wavy annular flow at $x = 82\%$ and $f_A = 0$ Hz; (g) smooth annular flow at $x = 82\%$ and $f_A = 0$ Hz.

4.3. Coalescence

Fig. 18 shows coalescence phenomena as described by f_A for eight different mass fluxes where the frequency of bubbles (small and/or elongated) that go past the observation point is plotted versus local vapor quality. The upward slope shows a dependency between the heat flux in the evaporator (or vapor quality) and the average frequency (count rate). The higher the heat flux is, the larger the average frequency. The average frequency then reaches a maximum and starts to decrease. The downward slope in average bubble frequency indicates the relative rate of coalescence. *Rate 1* refers to the zone of coalescence of small bubbles into elongated bubbles until no more small bubbles exist (a "best" line indicates this trend); *Rate 2* refers to the coalescence between elongated bubbles into even larger elongated bubbles or semi-annular flow (a "best" line also indicates this trend). The higher the mass flux, the higher are the slopes of *rate 1* and *rate 2*.

The second rate comprises two types of coalescence, one clean (slug flow) and the other one affected by the deformation of the rear of the bubbles that leads to semi-annular flow, but the rate stays the same. The *rate 2* tends to increase when increasing mass flux, meaning that slug/semi-annular flow tends to disappear as well as slug flow. But in our case, the mass flux is not high enough to reach this situation. Coalescence is one of the most important phenomena observed in this study because of its influence on flow pattern transitions as noted earlier.

4.4. Time averaged void fractions

It is possible to determine indirectly the cross-sectional void fraction by using the superficial vapor velocity given by Eq. (5) and the vapor bubble velocity obtained from the laser signals

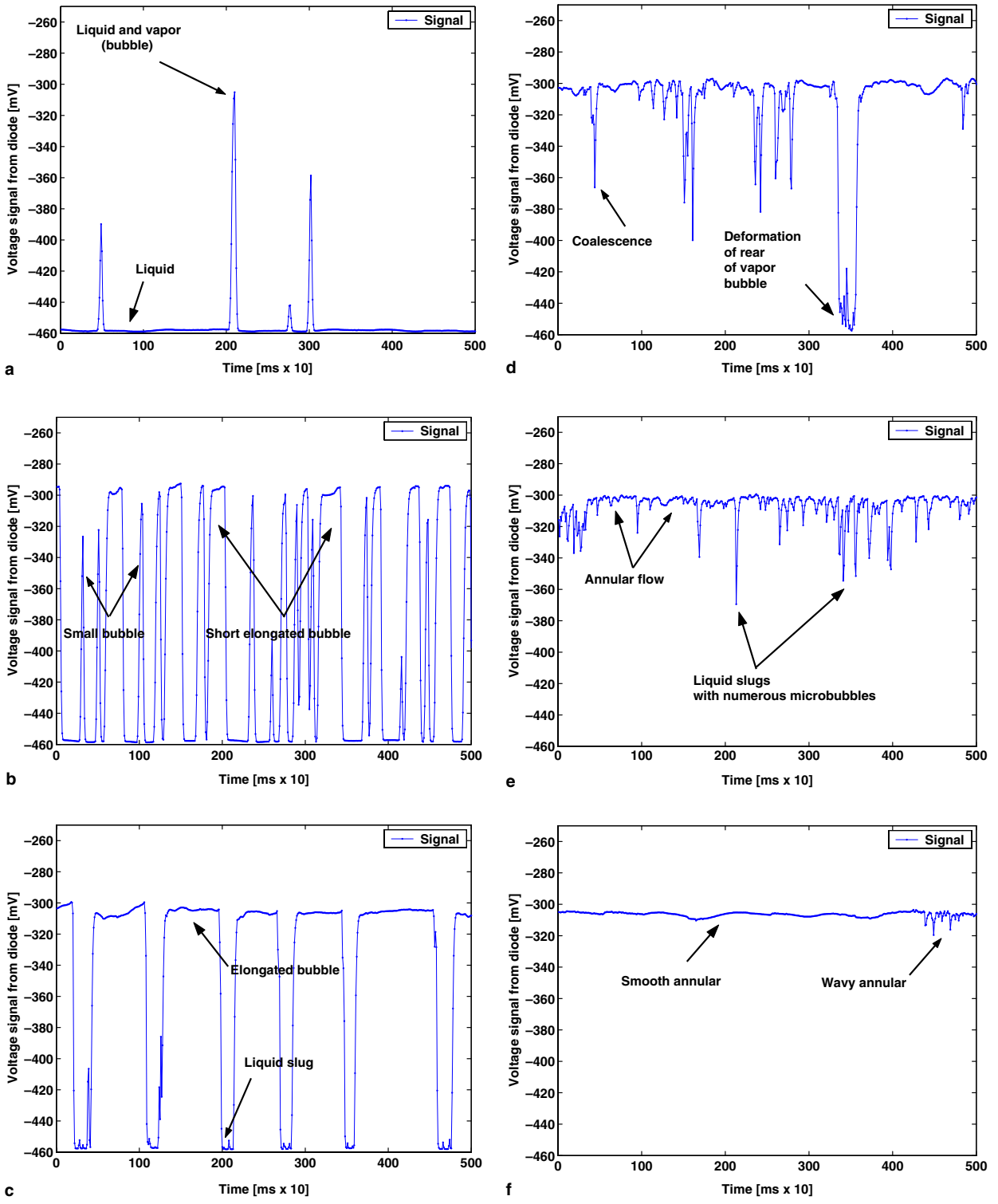

Fig. 15. Flow pattern laser signals for $D = 0.5$ mm, $L = 70.70$ mm, $G = 500$ kg m^{-2} s^{-1}, $T_{sat} = 30$ °C, $\Delta T_{sub} = 3$ °C: (a) bubbly flow signal at $x = 2\%$ and $f_A = 131$ Hz; (b) bubbly/slug flow signal for at $x = 4\%$ and $f_A = 520$ Hz; (c) slug flow signal at $x = 11\%$ and $f_A = 136$ Hz; (d) slug/semi-annular flow signal at $x = 19\%$ and $f_A = 33$ Hz; (e) semi-annular flow signal at $x = 40\%$ and $f_A = 0$ Hz; (f) annular flow signal at $x = 82\%$ and $f_A = 0$ Hz.

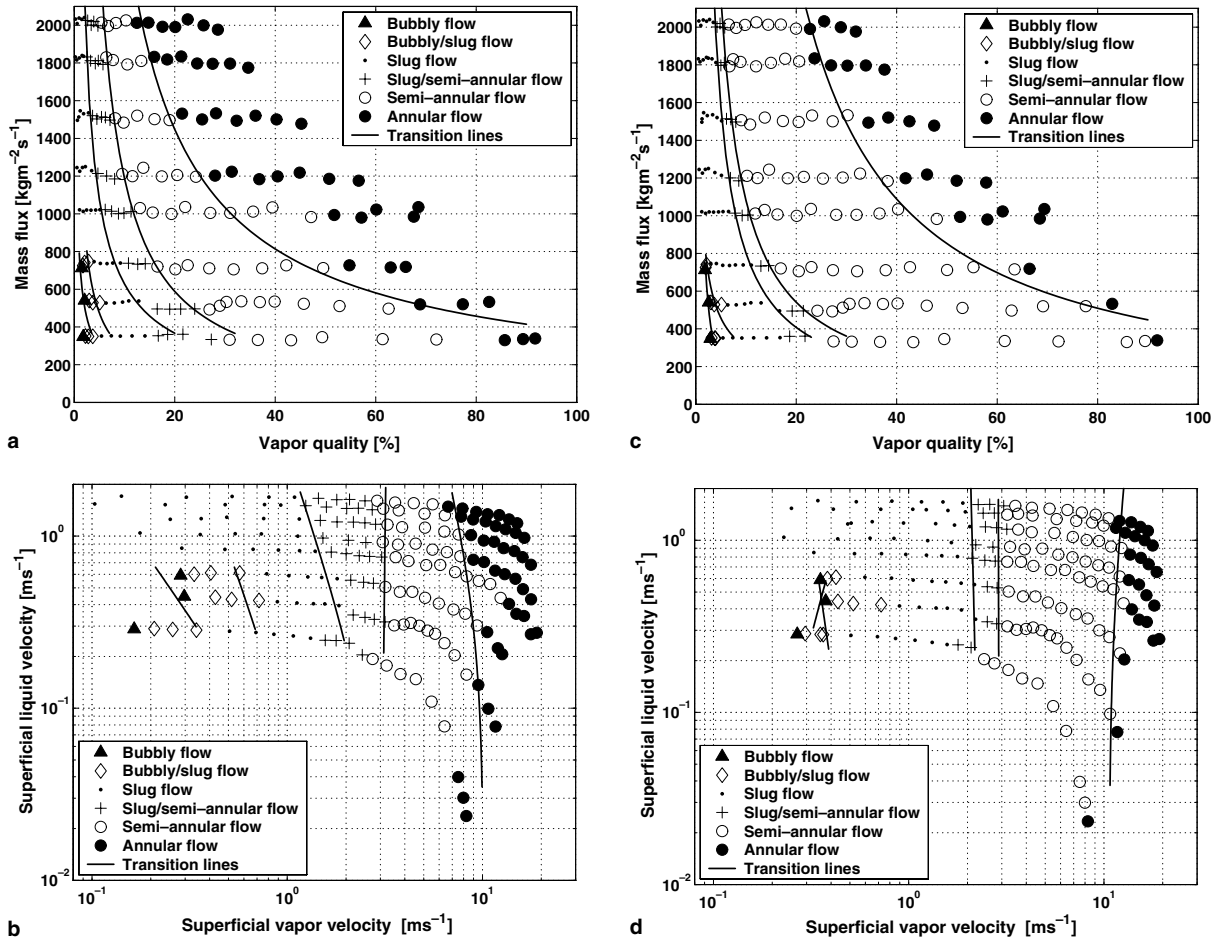

Fig. 16. Flow pattern maps with transition lines for $D = 0.5$ mm, $L = 70.70$ mm, $T_{sat} = 30$ °C, $\Delta T_{sub} = 3$ °C using the two lasers: (a) flow pattern observations from laser 1 with transition lines; (b) flow pattern map from laser 1 with transition lines; (c) flow pattern observations from laser 2 with transition lines; (d) flow pattern map from laser 2 with transition lines.

$$\varepsilon_G = \frac{J_G}{U_G} \tag{6}$$

where ε_G is the cross-sectional void fraction.

The time averaged centerline void fraction, on the other hand, is calculated by assuming that its value is 1 if there is vapor and 0 if liquid and then processing the signal accordingly. It does not take into account the radial distribution of the liquid and vapor but only that at the nose and rear of the bubble, i.e. essentially that at the centerline of the channel. When semi-annular flow is reached, it becomes 1 as expected and is used as a further quantitative check on that transition.

Fig. 19a shows the time averaged centerline (c-l) void fractions and the cross-sectional (c-s) void fractions from laser 1 versus the thermodynamic vapor quality. The cross-sectional void fractions are also compared to those predicted with the homogeneous model. For the same reason as for the velocity, the cross-sectional void fractions are close to the homogeneous void fraction for low vapor quality and then diverge. These results apply to slug and slug/semi-annular flow regimes occurring before semi-annular flow as indicated by the centerline void fraction reaching 1.0 at $x = 10.4\%$.

In Fig. 19b, the thus determined cross-sectional (c-s) void fractions are plotted versus the gas volumetric ratio defined by Eq. (7)

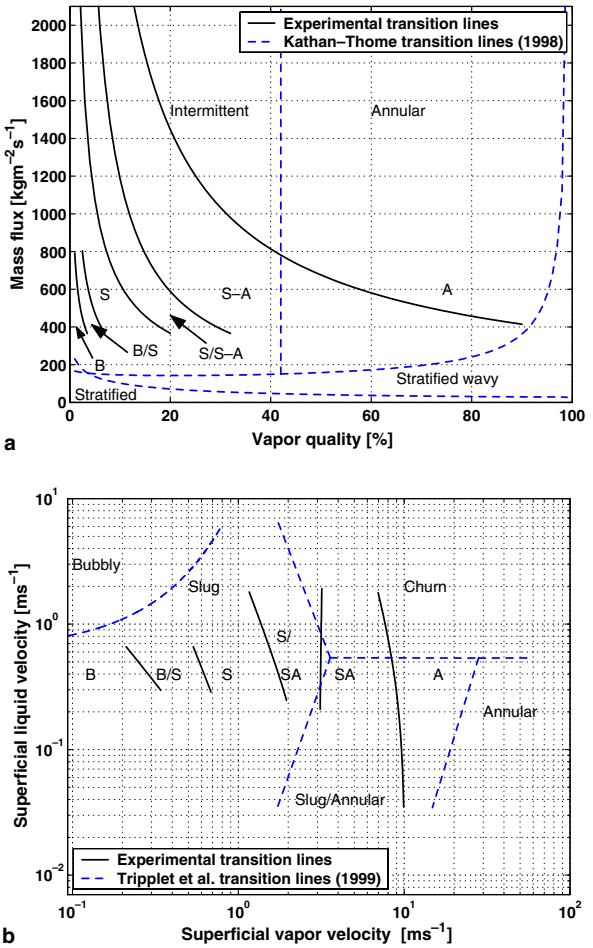

Fig. 17. Comparison between present flow pattern transition observations for $D = 0.5$ mm, $L = 70.70$ mm, $T_{sat} = 30$ °C, $\Delta T_{sub} = 3$ °C and two different flow pattern maps available for macro and microscale. (a) Comparison between present experimental transition lines from laser 1 and Kattan–Thome–Favrat macroscale map in a mass flux versus vapor quality format at the present test conditions (B = bubbly flow, B/S = bubbly/slug flow, S = slug flow, S/S-A = slug/semi-annular flow, S-A = semi-annular flow, A = annular flow). (b) Comparison between present experimental transition lines from laser 1 and Tripplet et al. transition lines available for air–water flow in a 1.097 mm tube diameter.

$$\beta = \frac{J_G}{J_G + J_L} \tag{7}$$

where β is the gas volumetric ratio.

4.5. Bubble lengths

The bubble lengths are calculated by using the vapor velocity and the time that a vapor bubble needs to cross the laser signal. Fig. 20 shows the mean bubble lengths versus vapor quality for four different mass fluxes. In bubbly flow, the bubble lengths are less than the diameter of the tube (horizontal black line). When semi-annular flow is reached, bubble lengths tend to infinity.

5. Conclusions

An optical measurement method has been developed to characterize flow pattern transition of two-phase flow in microtubes. It consists of shining two microlaser beams through a glass tube and the fluid at two

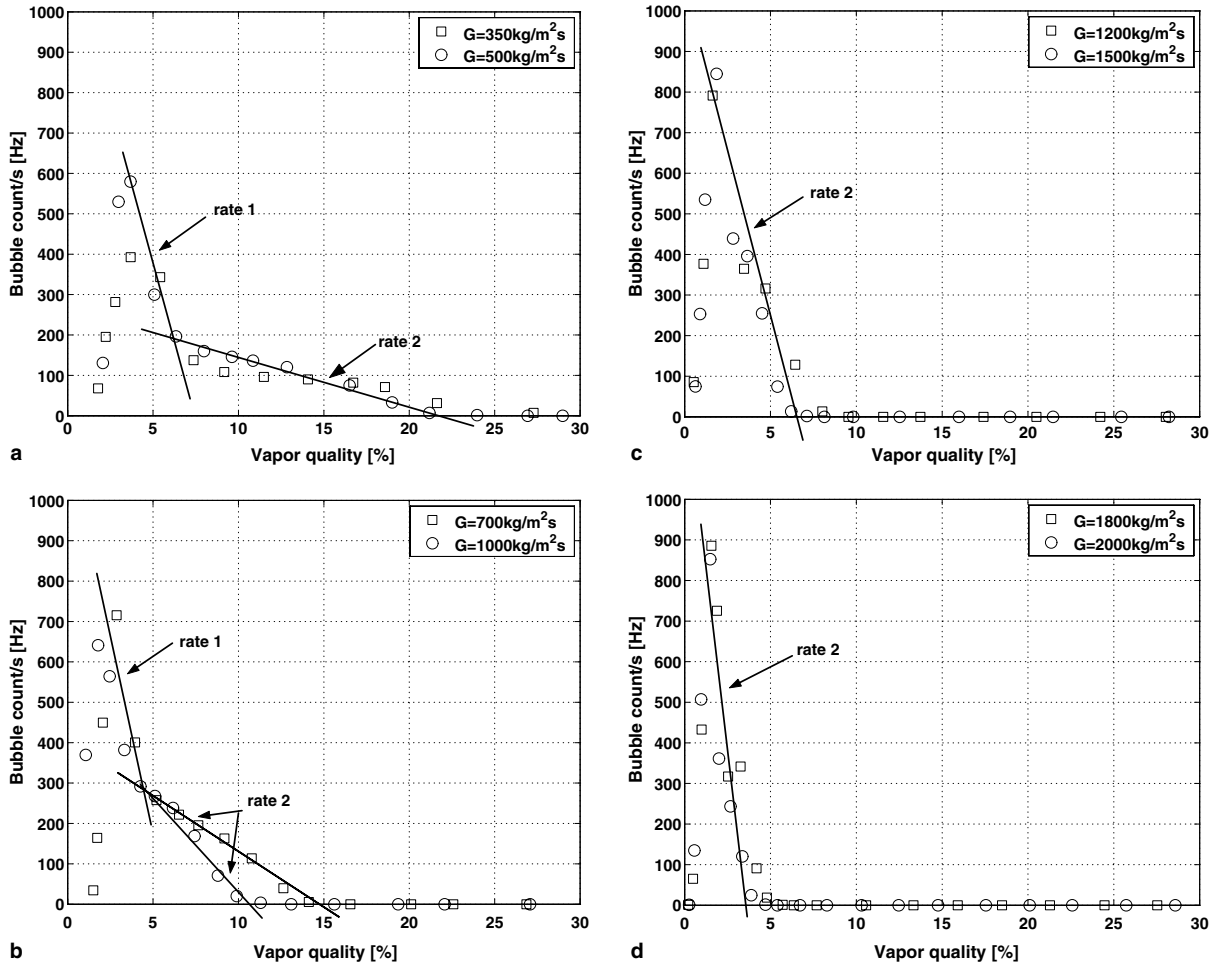

Fig. 18. Coalescence phenomena from laser 1 for $D = 0.5$ mm, $L = 70.70$ mm, $T_{sat} = 30$ °C, $\Delta T_{sub} = 3$ °C: (a) $G = 350$ kg m^{-2} s^{-1} and $G = 500$ kg m^{-2} s^{-1}; (b) $G = 700$ kg m^{-2} s^{-1} and $G = 1000$ kg m^{-2} s^{-1}; (c) $G = 1200$ kg m^{-2} s^{-1} and $G = 1500$ kg m^{-2} s^{-1}; (d) $G = 1800$ kg m^{-2} s^{-1} and $G = 2000$ kg m^{-2} s^{-1}.

different locations, using two lenses to focus the laser beams to the middle of the microtube, and using two photodiodes to recuperate the intensity of the light, whose signals are used to distinguish whether liquid, vapor or liquid and vapor are present in the cross-section. Bubble frequency, percentage of surviving small bubbles, lengths of bubbles and flow pattern transitions are parameters that are able to be determined by this technique. Mean vapor velocity is also calculable from the measurements at some test conditions.

Four principal flow patterns (bubbly flow, slug flow, semi-annular flow and annular flow) with their transitions (bubbly/slug flow and slug/semi-annular flow) are observed for the present experiments with R-134a in a 0.50 mm circular channel. Regime changes are detected by bubble frequency analysis combined with a small bubble coalescence study. The higher the mass flux is, the earlier annular flow is encountered. Bubbly flow tends to disappear at high mass flux because small bubbles quickly coalesce to form elongated ones. It is also possible to characterize the rate of bubble coalescence, which is identified here as an important phenomena in flow pattern transitions. Two types of coalescence exist depending on the presence of small bubbles or not. The higher the mass flux, the higher the elongated bubble coalescence rate is and the lower the small bubble coalescence rate is.

Void fraction, a very important parameter for heat transfer and pressure drop models, can also be evaluated, though one needs to carefully interpret the effects of non-homogeneous radial distribution of void fraction. Void fractions are only obtainable in slug and slug/semi-annular flows, where the results are found to be close to homogeneous flow values.

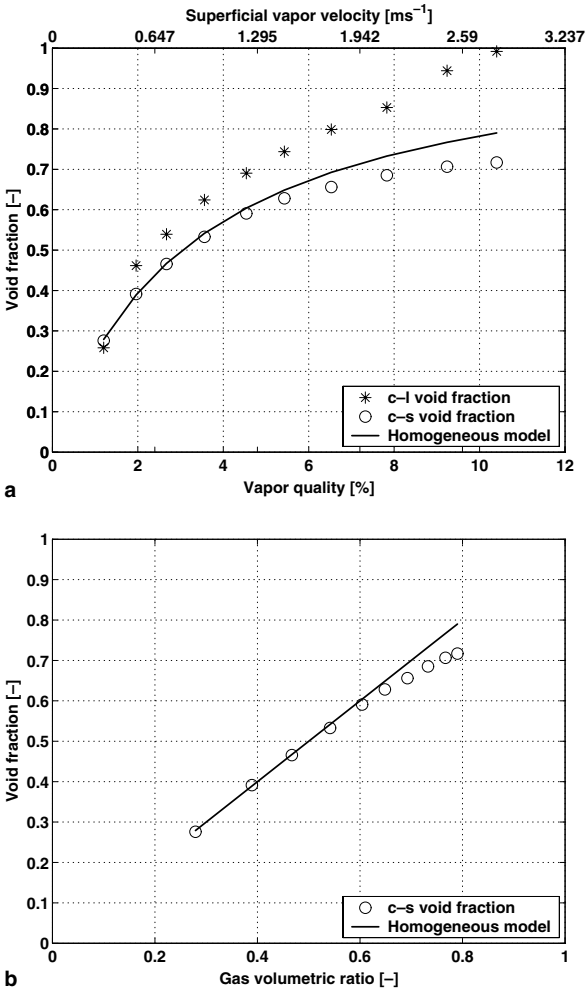

Fig. 19. Void fractions from laser 2 for $D = 0.5$ mm, $L = 70.70$ mm, $T_{sat} = 30$ °C, $\Delta T_{sub} = 3$ °C and $G = 1000$ kg m^{-2} s^{-1}.

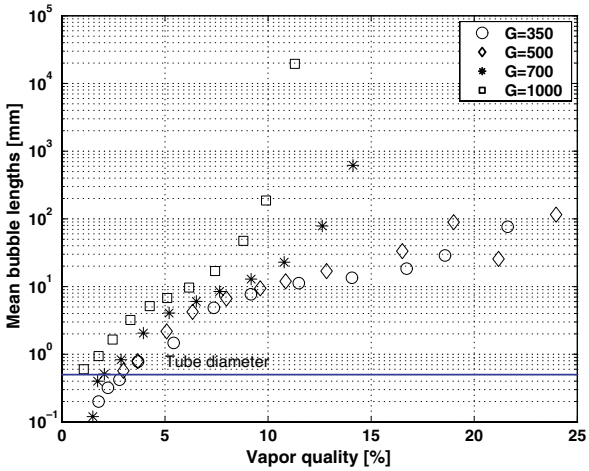

Fig. 20. Mean bubble lengths from laser 1 for $D = 0.5$ mm, $L = 70.70$ mm, $T_{sat} = 30$ °C, $\Delta T_{sub} = 3$ °C.

Acknowledgements

R. Revellin is supported by the European Community's Human Potential Programme under contract HPRN-CT-2002-00204, [HMTMIC] funded by OFES, Bern, Switzerland. V. Dupont was supported by Swiss National Fund (FNS) contract number 2000021-101597/1.

References

Armand, A.A., Treschev, G.G., 1946. The resistance during the movement of a two-phase system in horizontal pipes. Izv. Vses. Teplotek. Inst. 1, 16–23.

Cornwell, K., Kew, P.A., 1992. Boiling in small channels. In: Pilavachi, P. (Ed.), Proceedings of CEC Conference on Energy Efficiency in Process Technology. Elsevier, Athens, Greece, pp. 624–638.

Cubaud, T., Ho, C.-M., 2004. Transport of bubbles in square microchannels. J. Phys. Fluids 16 (12), 4575–4585.

Damianides, C.A., Westwater, J.M., 1988. Two-phase flow patterns in a compact heat exchanger and in small tubes. In: Proceedings 2nd UK National Conference on Heat Transfer, vol. 2. Glasgow, Scotland, pp. 1257–1268.

Dupont, V., Thome, J.R., Jacobi, A.M., 2004. Heat transfer model for evaporation in microchannels. Part 2: comparison with the database. Int. J. Heat Mass Transfer 47, 3387–3401.

Hetsroni, G., Mosyak, A., Segal, Z., Pogrebnyak, E., 2003. Two-phase flow patterns in parallel micro-channels. Int. J. Multiphase Flow 29, 341–360.

Kasza, K.E., Didascalou, T., Wambsganss, M.W., 1997. Microscale flow visualization of nucleate boiling in small channels: mechanisms influencing heat transfer. In: Shah, R. (Ed.), Proceedings of International Conference on Compact Heat Exchangers for Process Industries. Begell House, New York, USA, pp. 343–352.

Kattan, N., Thome, J.R., Favrat, D., 1998. Flow boiling in horizontal tubes: part 1 – development of a diabatic two-phase flow pattern map. J. Heat Transfer 120, 140–147.

Kawahara, A., Chung, P.M.Y., Kawaji, M., 2002. Investigation of flow pattern, void fraction and pressure drop in a microchannel. Int. J. Multiphase Flow 28, 1411–1435.

Kawahara, A., Sadatomi, M., Okayama, K., Kawaji, M., Chung, P.M.Y., 2005. Effects of channel diameter and liquid properties on void fraction in adiabatic two-phase flow through microchannels. Heat Transfer Eng. 26 (3), 13–19.

Kew, P.A., Cornwell, K., 1997. Correlations for the prediction of boiling heat transfer in small-diameter channels. Appl. Therm. Eng. 17, 705–715.

Lin, S., Kew, P.A., Cornwell, K., 1998. Two-phase flow regimes and heat transfer in small tubes and channels. In: Proceedings of II IHTC, vol. 2. Kyongju, Korea, pp. 45–50.

Lowe, D.C., Rezkallah, K.S., 1999. Flow regime identification in microgravity two-phase flows using void fraction signals. Int. J. Multiphase Flow 25, 433–457.

Matthes, W., Riebold, W., DeCooman, E., 1970. Measurement of the velocity of gas bubbles in water by a correlation method. Rev. Sci. Instrum. 41, 843–845.

Mertz, R., Wein, A., Groll, M., 1996. Experimental investigation of flow boiling heat transfer in narrow channels. Calore e Tecnol. 14, 47–54.

Serizawa, A., 2004. Multiphase flow in microchannels. In: The Second International Symposium on Multiphase, Non-Newtonian and Reacting Flows'04, September 10–12, Hangzhou, China.

Serizawa, A., Feng, Z.P., 2001. Two-phase flow in microchannels. In: ICMF. New Orleans, USA, keynote lecture.

Serizawa, A., Takahashi, O., Zawara, Z., Komeyama, T., Michiyoshi, I., 1990. Heat transfer augmentation by the two-phase bubbly flow impinging jet with a confining wall. In: International Heat transfer Conference, pp. 93–98.

Serizawa, A., Feng, Z., Kawara, Z., 2002. Two-phase flow in microchannels. Exp. Thermal Fluid Sci. 26, 703–714.

Sheng, C.H., Palm, B., 2001. The visualization of boiling in small-diameter tubes. In: Heat Transport and Transport Phenomena in Microsystems. Banff.

Steinke, M.E., Kandlikar, S.G., 2003. Flow boiling and pressure drop in parallel flow microchannels. In: 1st International Conference on Microchannels and Minichannels, Rochester, USA, pp. 1–12.

Suo, M., Griffith, P., 1964. Two-phase flow in capillary tubes. J. Basic Eng., 576–582.

Thome, J.R., Dupont, V., Jacobi, A.M., 2004. Heat transfer model for evaporation in microchannels. Part 1: presentation of the model. Int. J. Heat Mass Transfer 47, 3375–3385.

Triplett, K.A., Ghiaasiaan, S.M., Abdel-Khalik, S.I., Sadowski, D.L., 1999. Gas–liquid two-phase flow in microchannels. Part I: two-phase flow patterns. Int. J. Multiphase Flow 25, 377–394.

Wambsganss, M.W., France, D.M., Jendrzejczyk, J.A., Tran, T.N., 1993. Boiling heat transfer in a horizontal small-diameter tube. J. Heat Transfer 115, 963–972.

Xu, J., Gan, Y., Zhang, D., Li, X., 2005. Microscale boiling heat transfer in a micro-timescale at high heat fluxes. J. Micromech. Microeng. 15, 362–376.

Yang, C.Y., Shieh, C.C., 2001. Flow pattern of air–water and two-phase r-134a in small circular tubes. Int. J. Multiphase Flow 27, 1163–1177.